

THERMAL STRUCTURE OF THE ATMOSPHERIC BOUNDARY LAYER ON MARS BASED ON MINI-TES OBSERVATIONS

Zbigniew Sorbjan^{1,2,3*}, Michael Wolff³, and Michael D. Smith⁴

¹Marquette University, Milwaukee, WI, ²Institute of Geophysics, Polish Academy of Sciences, Warsaw, Poland, ³Space Science Institute, Boulder, CO, ⁴NASA Goddard Space Flight Center, Greenbelt, MD

ABSTRACT: This paper presents and discusses the vertical profiles of the potential temperature in the Martian boundary layer. The profiles were remotely sensed from on-board the Spirit Mars Exploration Rover during the first 702 sols of its operation in 2004-2005. The rover carried the Miniature Thermal Emission Spectrometer (Mini-TES), which allowed it to retrieve temperature profiles up to a level 2-km above the ground surface. The data analyzed here permit a reconstruction of the diurnal and seasonal structure of the lower part of the Martian convective boundary layer, an evaluation of the boundary layer depth, and a computation of the temperature heat flux.

KEY WORDS: Atmospheric boundary layer on Mars, depth of Martian convective boundary layer, Mini-TES observations, potential temperature on Mars, turbulent heat flux on Mars

Submitted on 5 February 2009, revised on 10 June 2009

1. Introduction

A basic understanding of near-surface turbulence on Mars has been obtained from in-situ measurements first performed by two Viking Landers, and subsequently by the Mars Pathfinder Lander (e.g., Smith, 2008). The Viking-1 Lander arrived on Mars at 16:00 in the afternoon of 20 July 1976, at (22°N, 48°W). The Viking-2 touched down at 09:45 in the morning of 3 September

* Correspondence to: Z. Sorbjan, Physics Dept., Marquette University, Milwaukee, WI 53201, PO Box 1181, USA.
E-mail: zbigniew.sorbjan@mu.edu

1976, at (48°N, 225°W). Both Viking landers recorded the air temperature, wind velocity, and atmospheric pressure on a single level of 1.6 m above the ground surface (e.g., Sutton et al., 1978; Tillman et al., 1994). The Mars Pathfinder, which landed 21 years later (on 4 July 1997) at (19°N, 33°W), had an improved instrumentation package, with higher sensitivity and temporal resolution (e.g., Schofield et al., 1997; Wilson and Joshi, 2000). It included a pressure sensor, a hot-wire anemometer that measured both speed and direction, and three thermocouples, placed at three levels (0.59, 0.84, and 1.34 m) above the underlying surface.

In 2005, the Mars Exploration Rover (MER) missions brought the next two spacecrafts to the surface of Mars. The Spirit rover landed in Gusev Crater (14.6°S, 184.5°W) on 4 January 2005 (seasonal longitude $L_s = 328^\circ$). The Opportunity rover followed three weeks later ($L_s = 339^\circ$), arriving on Meridiani Planum (1.9°S, 2.5°W). Each rover carried the Miniature Thermal Emission Spectrometer (Mini-TES), allowing for remote retrieval of temperature profiles in the lowest 2 km of the Martian atmosphere (Smith et al., 2004; Smith et al., 2006; Spanovich et al., 2006).

Prior to the Mars Exploration Rover (MER) missions, information on the vertical structure of the atmosphere at levels, extending deeper into the Martian boundary layer, has been scarce. Measurements of atmospheric pressure as a function of height were made by each of the two Viking landers during their entry and descent phases. The third profile was provided during the entry of the Pathfinder mission. Radio occultation observations by Mariner 9 (Kliore et al., 1973), data from the Viking orbiters (Lindal et al., 1979), the Mars Global Surveyor (Hinson et al., 1999, 2001), and the Mars Express (Hinson et al., 2008) resulted in a remote evaluation of a number of boundary layer profiles, but these were scattered in time and location and did not have sufficient vertical resolution to probe details of the boundary layer. The Thermal Emission Spectrometer (TES) on board the Mars Global Surveyor was also used to retrieve the spatial and temporal distribution of temperature from orbit (Christensen et al., 2001). These data had a more systematic seasonal and spatial sampling. Vertical resolution, however, was too low to resolve the boundary layer at all. Numerical simulations of the Martian boundary layer provided some more detailed information (e.g., Savijärvi et al., 2004; Rafkin et al., 2001; Toigo et al., 2003; and Michaels and Rafkin, 2004), but these computations could not be properly verified prior to the

arrival of the MER Spirit and Opportunity rovers on the surface of Mars. The post-MER, Phoenix mission, which landed on May 22, 2009, obtained both entry-descent-landing data, as well as surface measurements of pressure, temperature, and winds. Its information, however, is not yet available in a peer-reviewed format.

The results of the Mini-TES temperature retrievals from both the Spirit and Opportunity rovers were described by Smith et al. (2004, 2006) and by Spanovich et al. (2006), with some additional facets to the retrieval considered by Wolff et al. (2006). Savijärvi and Kauhanen (2008) analyzed both Mini-TES data sets, and compared the obtained profiles with a one-dimensional boundary-layer model. In this paper, we extend the MER analyses with a more focused study of the temperature profiles in the lower portion of the Martian boundary layer, obtained from on-board the Spirit rover during the first 702 days (just over one Martian year) of its operation. We include an evaluation of the diurnal and seasonal variations of the potential temperature profiles, the estimation of the depth of the Martian boundary layer, and the computation of the turbulent heat flux.

The paper has the following structure. The temperature retrieval method, which constitutes a slightly improved form of the original retrieval procedure described by Smith et al. (2006), is introduced in Section 2. The selected temperature profiles are discussed in Section 3. More specifically, the diurnal and seasonal variations of the potential temperature are discussed in Section 3.1. In Sections 3.2 and 3.3, we assess the daytime growth of the convective boundary layer, and provide examples of the retrieved heat flux. Final remarks are outlined in Section 4.

2. Temperature retrievals

The Mini-TES is a Fourier transform spectrometer, which can collect thermal infrared spectra in 167 channels between 5 and 29 μm , within a narrow angle of 20 mrad, at any elevation angle up to 30° above the plane of the rover deck. Spectra can be acquired every 2 seconds through the top of the Pancam Mast Assembly, which can rotate by a full angle of 360° in azimuth. The retrieval procedure, and information on the availability of upward-looking Mini-TES observations from the Spirit and Opportunity Mars Exploration Rovers, were previously presented by Smith et al. (2006) and Smith (2008). Christensen et al., (2004) provided additional

instrument details. Uncertainty in the retrieved temperatures is about 2 K near the surface, increasing to 4 K at 2 km.

In contrast to earlier presentations of Mini-TES measurements, all profiles analyzed in this paper are expressed in terms of the potential temperature, Θ , which remains conserved during adiabatic vertical motions, and is unaffected by pressure changes during the lifting or sinking of air during Martian convection. We use the following definition of the potential temperature:

$$\Theta = T \left(\frac{p_o}{p} \right)^\alpha \quad (1)$$

where T is the actual absolute temperature at a given pressure level, p , and p_o is the current surface pressure (note that the surface pressure is not constant with time and that it has an annual cycle), evaluated based on results from a global circulation model (Smith et al., 2006), the gas constant is $R = 191 \text{ J}/(\text{kg K})$, $c_p = 736 \text{ J}/(\text{kgK})$ is the specific heat at constant pressure, and $\alpha = R/c_p = 0.2595$. It should also be noted that based upon numerical experiments performed by Smith et al. (2006), perturbations of ± 1 mbar produce changes in the retrieved temperatures below the 1 K level. Furthermore, the robustness of the surface pressure field from global circulation models has been validated against Viking and Pathfinder measurements by several authors (e.g., Haberle et al., 1993a; Hinson et al., 1999 and references within).

At the underlying surface, the potential and the actual temperature coincide. Within the first 2 km above the surface, the potential temperature gradient is approximately equal to: $d\Theta/dz \approx dT/dz + \gamma_a$, where $\gamma_a = g/c_p = 4.5 \text{ K}/\text{km}$ is the dry adiabatic lapse rate for the Martian atmosphere, and g is the gravity acceleration. During daytime convection, the potential temperature decreases (super-adiabatic stratification), or is constant (well-mixed) with height. During nocturnal conditions, temperature inversion (sub-adiabatic stratification) is developed near the surface, with the potential temperature increasing with height.

As an example, Figure 1a shows the potential temperature profiles obtained on sol 53 by the Spirit rover (where “sol” is a Martian solar day, which is about 2.7% longer than it is on Earth). For that time, the seasonal heliocentric longitude L_s (which indicates the position of Mars

in its orbit around the Sun) was 356° , or just before Fall Equinox in the Southern Hemisphere. The profiles in the figure were retrieved at the elevation angle β of 26° , beginning at 8:50 of the Martian local true solar time (LTST, which is a function of the solar hour angle at the landing site on Mars). The LTST is referenced to a 24-hour "Martian clock", with "hours" and "minutes" that are 2.7% longer than their standard durations on Earth. However, the use of "seconds" in this paper refers to the standard terrestrial unit.

The profiles in Figure 1 are 2-second averages plotted every 100 s. The profiles in Figure 1a were obtained by using the original retrieval procedure described by Smith et al. (2006). Each profile in the figure shows a multi-level structure. It consists of a super-adiabatic, 50-meter layer, located just above the ground. Above it, there is a sub-adiabatic layer, about 75 m deep. The sub-adiabatic layer is covered by a 200-meter layer of a nearly constant potential temperature, and an inversion layer above it. The retrievals indicate that the potential temperature in the boundary layer gradually increases with time, primarily as a result of radiative forcing.

The vertical structure of the Martian surface layer in Figure 1a appears to be too complex, given the current understanding of boundary layer dynamics (e.g., Sorbjan 2007a, b). Specifically, the local minima at about 50 m above the ground, and the local maxima at about 125 m, seem to be artifacts of the applied retrieval procedure. Although the figure illustrates an extreme example, it is a reminder of the fact that the Smith et al. (2006) retrieval algorithm uses a temperature profile from the Thermal Emission Spectrometer (TES) on-board the Mars Global Surveyor (MGS) as the "initial guess" of the desired solution. Even during the portion of the mission, before the loss of TES temperature profiles (31 August 2004), when spatial proximity could provide some degree of co-location, the MGS orbit allowed only temperature profiles characteristic of about 2:00 and 14:00 LTST. As a result, the initial guess for the results of Figure 1a represented thermal conditions significantly different from those observed by Mini-TES. Although this issue was explored briefly by Wolff et al., (2006), their interest was primarily that of the effect on the retrieved optical depths.

In this paper, we applied a simple modification to the original Smith et al. (2006) algorithm. Note that the "sinusoidal" structure in the profiles of Figure 1a is suggestive of an over-correction near the surface from the initial 14:00 LTST profile. The algorithm returns temperatures near the surface as a reasonable fit for the core of the $15\ \mu\text{m}$ band, but as a poor fit

(too cold) in the wings of the band. The retrieval subsequently compensates by “warming” the atmosphere above the peak of the contribution functions from the core of the 15 μm band, i.e., extra radiance to improve the fit in the wings, with essentially no change to the band core. This oscillation damps out quickly, but not before leaving a signature that is outside of the expected precision of the returned profile. If the above behavior is the result of the initial guess being “too far” from actual conditions, a logical step would be to run the retrieval again, but in this case, one substitutes the profile from the initial Mini-TES for that of the TES profile. In other words, one carries out a second iteration of the temperature retrieval algorithm where the initial guess is now the retrieved profile from the first iteration. The resulting temperature profiles are displayed in Figure 1b. As might be expected, the modified profiles do not possess the questionable vertical structure seen in Fig.1a. Instead, they offer the more straightforward interpretation of the presence of a shallow, super-adiabatic sub-layer located just above the ground, followed by a relatively thin mixed layer, and the inversion layer above it.

Although we employ four iterations in our modification of the retrieval algorithm (each time, using the previous result of the initial guess), the resulting profiles have typically reached convergence as determined by the precision specified by Smith et al. (2006) by the second iteration. The correction changes the retrieved temperatures by a relatively small amount (about ± 2 K in Figure 1b), and the change is only significant when looking at vertical gradients, and at observations taken during the early and mid-morning.

In addition, it should be mentioned that the Mini-TES temperature retrievals can have some sensitivity to the value of the elevation angle, β . The elevation angle is constrained to be no larger than 30° above the rover deck, though the elevation angle above the local gravitational horizontal surface can be larger than 30° , when the rover is on sloped terrain. In Figure 2, we present three profiles of the potential temperature on sol 7, obtained for different elevation angles $\beta = 10^\circ$ at 13:04 LTST, $\beta = 20^\circ$ at 13:09, and $\beta = 30^\circ$ at 13:13 LTST. All the profiles coincide within the 100-m layer above the ground. The profile, obtained at the elevation angle of 10° , immediately increases with height above the level of 200 m. The second profile indicates the presence of a shallow, well-mixed layer of about 200 m deep. The third profile includes a deeper well-mixed layer of about 1000 m deep. Above the 1500 m level, the temperature lapse rate is the same for all three profiles, and the potential temperature difference between the first and the

third profiles is about 4 K.

In this paper, we will use only temperature profiles retrieved from observations taken at relatively high elevation angles (20° or higher) since they have the smallest uncertainties and horizontal averaging. Note that observations taken at higher elevation angles were frequently collected for a variety of local times during the first 420 sols of the mission. However, between sols 420 and 550 ($L_s = 173^\circ$ to 250°), there is a complete lack of observations taken between 11:00 and 15:30 LTST. After sol 550, such observations remain relatively rare until sol 610 ($L_s = 290^\circ$).

3. Results

3.1. Temperature profiles

3.1.1. Diurnal effects

Most of the temperature profiles analyzed in this paper are based on observations performed during the daytime. Due to technical constraints (e.g., high energy costs associated with heating of the instrument and other spacecraft components for nighttime operations), only a few nighttime observations were collected in the period from $L_s = 330^\circ$ to 60° , and only three between $L_s = 120^\circ$ and 300° (Smith et al., 2006). We have limited our analysis to profiles retrieved from 100-second samples, and to the lower 3km of the retrieval. It should be noted, however, that the Mini-TES spectra provide the most useful information only in the 2-km layer above the ground. The vertical resolution of the retrievals is smaller (\sim few meters) near the surface, but decreases rapidly (\sim few hundred meters) at the top of this domain.

Typical daytime profiles of the potential temperature are depicted in Figure 3a. The profiles in the figure were obtained in the interval between 8:50 and 16:31 LTST on sol 53 ($L_s = 356^\circ$, late summer). Note that on sol 53, sunrise and sunset occurred at 5:58 and 18:01 LTST, respectively. The morning profile at 8:50 is nearly linear with height, increasing from about 203 K near the surface ($z = 20$ m) to about 220 K at the level of 2 km. The resulting temperature

inversion is characterized by the potential temperature gradient $\Gamma \approx 8.5$ K/km. For comparison, the results obtained by Hinson et al. (2008) indicate that $\Gamma \approx 3.5$ K/km in the upper part of the atmosphere.

The subsequent profiles gradually migrate in time toward larger values of temperature. Near the surface, the process is caused by radiative effects and convection generated by the hot underlying surface. Convection causes the potential temperature to become more uniform with height, and the temperature gradient Γ to decrease in time.

By 9:59 LTST, a shallow super-adiabatic layer has formed near the surface. The layer is characterized by a sharp, nearly 5 K-temperature drop of the potential temperature with height within the first 150 meters above the ground. Above it, a shallow well-mixed layer of a constant potential temperature can be noticed, extending up to a level of about 250 m above the surface. In this layer, convection is likely to be organized in the form of regular cells (free convection) or rolls (forced convection) (e.g., Sorbjan, 2007 a, b). The temperature inversion above this layer is characterized by a gradient of about $\Gamma \approx 5$ K/km. The profiles at 9:59 and 10:14 LTST imply that the radiative heating at the surface is already quite intensive. In this 15-minute interval, the near-surface temperature increases from about 218 K to about 222 K, i.e. by 16 K per hour.

Between 12:54 and 13:01 LTST the increase of temperature near the surface is about 17 K/h. The depth of the super-adiabatic layer does not change in time and remains equal to about 150 m. The potential temperature gradient in the super-adiabatic layer reaches the maximum value at about 13:00 LTST, and then gradually decreases. At 16:31, the super-adiabatic layer near the surface is only weakly apparent, which indicates that the Sun at that time is close to the horizon. The potential temperature is nearly constant in height throughout the lowest 3-km of the atmosphere. As the surface temperature decreases, the depth of the convective boundary layer quickly decreases, as thermals are unable to penetrate high into the atmosphere.

Figure 3b depicts profiles of the potential temperature, which decreases with time during afternoon and nocturnal hours. The figure is composed of profiles obtained during a 3-week period, on sols 49, 53, 55, 65, and 70 (L_s in the range from 354° to 5°), in the interval from 16:31 to 9:00 LTST. The profiles in the figure are not substantially different from those that would be observed during a single night within the considered period of time.

The presence of a weak super-adiabatic surface layer at 16:31 LTST in Figure 3b indicates that convection is still active. Three quarters of an hour later, at 17:16, the temperature

inversion layer appears near the ground, even though the Sun is still above the horizon. The surface inversion layer at 17:16 LTST is about 200 m deep, and its strength at the surface is about 4 K. At 18:29, the surface inversion layer, defined by the non-linear portion of the temperature profile, deepens to about 600 m, and its strength increases to about 16 K. Above this layer, the potential temperature gradient is about $\Gamma = 1.5$ K/km. After midnight (i.e. at 1:23 and 4:56 LTST), the potential temperature gradient above the level of 1 km is nearly constant with time. At 1:23 LTST, the surface inversion reaches the level of 1000 m, and its strength at the surface is about 25 K. Above 1000 m, the temperature gradient is about 6 K/km, which is quite close to the gradient of 7 K/km at 8:50 LTST in Figure 3a. The profile at 4:56 has a similar shape, but is "shifted" toward lower temperatures above the level of 100 m. Below it, the temperature profile seems to be already affected by the heating energy of the rising Sun.

After sunrise, the increased infrared heating and convective mixing annihilates the 600-m deep surface inversion, as indicated by the profile at 9:00 in the figure. Above the level of 600 m, the temperature profiles remain unchanged in the interval from 4:56 until 9:00, as a result of the radiative equilibrium.

The near-surface air temperature of 187 K at 4:56 LTST, in Figure 3b, is presumably close to the minimum temperature, which occurs about sunrise. The near-surface temperature of 250 K at 16:31 LTST is close to the maximum temperature. Thus, the diurnal amplitude near the surface is about 65 K. The cooling rate in the interval from 16:31 to 4:56 LTST at the surface is about 5 K/h. The cooling rate at the level of 2 km is about -2.5 K/h, in the same interval of time.

The early autumn profiles in Figure 3b can be compared with the profiles in Figure 4, obtained about 100 sols later, during late fall, on sol 180 ($L_s = 57^\circ$). On that day, sunrise and sunset occurred at 6:28 and 17:32 LTST, respectively. The figure indicates that the cooling rate near the surface is about 5 K/h in the interval from 15:13 to 0:44 LTST, nearly the same value as in Figure 3b. The cooling rate at the level of 2 km is about 1.4 K/h in the same interval of time. The gradient of the potential temperature above the level of 1 km changes in time from about $\Gamma = 1.5$ K/km at 15:31, to $\Gamma = 6$ K/km at 0:44 LTST.

Figure 5 shows the temporal distribution of the potential temperature at three levels: $z = 20$ m, and the levels of 1 km and 2 km above the surface. The data points in the figure are based on the potential temperature profiles, plotted in Figures 3. The curves in the figure resemble slightly deformed sine functions, with a period of 24 hours. It should be pointed out that the plot

includes information about thermal stratification, and thus differs from analogous plots of the absolute temperature, presented by Spanovich et al. (2006), Smith et al. (2006), and Savijärvi and Kauhanen (2008). As a result of convective mixing, the maximum potential temperature near the surface is only by about 5 K higher than it is at the level of 1 km. Due to lack of convective mixing at night, the values of the potential temperature at these two levels are significantly different before sunrise. Note that plots of the absolute temperature (e.g., Smith et al., 2006) indicate opposite behavior: the largest temperature contrast is observed in the afternoon, and the smallest around sunrise.

The warming interval at the lowest layer in Figure 5 lasts about 9 hours, from about 6:00 to 15:00 LTST. The cooling interval is about 15 hours long, from about 15:00 to 6:00 LTST. Above, at the levels of 1 and 2 km, the warming period is about 11 hours long, from 6:00 to 17:00 LTST, while the cooling period is about 13 hours long and lasts from about 17:00 to 6:00 LTST. The peak-to-peak amplitude near the surface is about 60 K. The amplitude decreases with height, and is equal to 36 K at 1 km, and 26 K at 2 km.

At the level of 1 km, the maximum air temperature is observed at about 17:00 LTST. Near the surface, it occurs at about 15:00, which roughly agrees with Haberle et al. (1993a, b). As shown by Smith et al. (2006) and Spanovich et al. (2006), the maximum soil temperature is observed at local noon. Thus, there is a lag between the occurrence of the diurnal maximum near the ground and in the atmosphere just above it. Such a lag is primarily due to lower thermal inertia of Martian soil (expressed by a short time needed to reach thermal equilibrium) with respect to the atmosphere. Thus, the surface temperature almost instantly reacts to the level of solar insolation, which is directly related to solar altitude. Nevertheless, the heat transport to the atmosphere is small, due to low density of air, as opposed to the situation on Earth.

The minimum temperature near the surface occurs at about 6:00 LTST, which agrees with Haberle et al. (1993b). The exact moment of the minimum temperature at the levels of 1 and 2 km cannot be evaluated from the figure because of lack of observations. One can expect, however, that since cooling is enforced radiatively, the minimum temperature should occur at about the same time at all levels. Note that cooling is most intense at the surface, and that the minimum temperature near the surface is about 25 K lower than at the level of 2 km.

3.1.2. Seasonal effects

Before we examine the seasonal effect, it is useful to remind that Mars's axial angle of 25.2° is very close to the value of 23.45° for Earth. As a result, the planet has four seasons in a year (which is 669 sols long), as on Earth. The Vernal Equinox (beginning of Autumn at the Southern Hemisphere -- Spirit site) occurs at $L_s = 0^\circ$, the Southern Hemisphere Winter Solstice is at $L_s = 90^\circ$, the Southern Hemisphere Spring Equinox is at $L_s = 180^\circ$, and the Southern Hemisphere Summer Solstice is at $L_s = 270^\circ$ (e.g., Smith, 2008). The orbital eccentricity of Mars (0.093) is significantly greater than that on Earth. Mars is closest to the Sun (perihelion) at $L_s = 251^\circ$, when it is late Spring in the Southern Hemisphere, and farthest from the Sun (aphelion) at $L_s = 71^\circ$, during late Southern Fall. As a result, the Martian seasons are of unequal length, much more so than on the Earth. Summers in the Southern Hemisphere are relatively short (154 sols) and warm. Winters are relatively long (179 sols) and cold, as Mars is moving more slowly near aphelion. Southern autumn is 193 sols long, while Southern spring lasts 143 sols.

Seasonal variation of the potential temperature profiles is presented in Figure 6. Profiles in the figures were obtained in approximately ± 1 hour intervals at around 13:00, and around 16:00 LTST. Profiles at around 13:00 are shown in Figure 6a only in a period from sol 7 to 424, because observations at larger elevation angles were not collected at that local time for sols 425-702. Profiles at around 16:00 LTST are shown in Figure 6b, in the period from sol 62 to 702.

The profiles in Figure 6a evolved toward lower temperatures during the period from sol 7 ($L_s = 329^\circ$, summer) to sol 275 ($L_s = 100^\circ$, early winter), and then became warmer again during the interval from sol 275 to sol 424 ($L_s = 167^\circ$, late winter). Likewise, the profiles in Figure 6b evolved toward lower temperatures during the period from sol 62 ($L_s = 358^\circ$, summer) to sol 240 ($L_s = 83^\circ$, late fall), became warmer during the interval from sol 240 to sol 484 ($L_s = 202^\circ$, spring), and finally cooled again during the interval ending at sol 702 ($L_s = 337^\circ$, summer). Note that in Fig. 6b, the profiles for sols 62 and 702 coincide, because their seasonal dates are nearly the same.

At around 13:00 LTST, the surface super-adiabatic layer near the surface is about 150-

200 m deep, over the entire course of the year, and its strength changes from about 7 K on sol 275, to 10 K on sol 424. The depth of the surface super-adiabatic layer at 16:00 is also about 150-200 m, but its strength is smaller, about 3 K. The profiles in Figure 6a are more uniform with height (“well-mixed”) in the 3-km layer than those in Figure 6b.

In Figure 7, we show the temporal distribution (over one Martian year) of the potential temperature observed at about 16:00 LTST at three levels: 20, 1000 and 2000 m above the surface. The temperatures in the figure exhibit one maximum and one minimum within the Martian year. The curves representing the potential temperature at various levels are approximately parallel, and asymmetric during the course of the Martian year. We find a quite good agreement in the temperatures at the beginning of years 1 and 2, except during a few first sols of each year, for which the retrieved atmospheric temperatures differed by about 5 K. We also detected some anomalies (perturbations) in the potential temperature in the interval between sols 500 and 700, which are not visible in the Figure 7, as only selected points appear in the presented plot. The described differences are most likely associated with large dust-storm events.

3.2. Mixed layer depth

In order to assess the vertical growth of the Martian convective boundary layer, we first estimate the level of free convection, h_c , which can be reached by thermals moving upward from the surface until their buoyancy vanishes. As shown by a dotted line in Figure 3a, thermals at the initial temperature (at the surface) of 218 K at 9:59 LTST would reach the altitude of about $h_c = 1200$ m, if they could move instantaneously. However, because atmospheric temperature increases with time and because thermals move with finite velocity, the above value of h_c would be overestimated. Assuming that the velocity of updrafts w_* near the surface is about 1-2 m/s (Sorbjan, 2007a), we can estimate that the travel time from the surface to the level 1200 m is about 10-20 minutes. Thus, before a thermal arrives at the level h_c , the atmospheric temperature will increase, and consequently, thermals will lose their buoyant push earlier. Note that the dotted line in Figure 3a crosses the 10:14 profile at the level of about $z = 900$ m. Consequently, we will estimate that the height of free convection at 10:14 is $h_c \sim 900$ m.

Referring again to Figure 3a, one can notice that the profiles at 12:54 and 13:01 LTST look like typical well-mixed profiles of the potential temperature on Earth, with one significant difference. They do not show the characteristic temperature jump present at the top of the mixed layer on Earth. This jump in potential temperature, $\Delta\Theta$, is typically a few degrees in the terrestrial atmosphere and is associated with thermals impinging at the top of the mixed layer. The resulting entrainment brings the warm air from the free atmosphere into the mixed layer while detrainment cools the interfacial layer.

The lack of a jump in the observed potential temperature profiles at the top of the Martian boundary layer could be associated with insufficient accuracy and vertical resolution of Mini-TES retrievals. We do not believe, however, that this factor is the main cause of the phenomenon -- as implied by large-eddy simulations of Martian convection by Sorbjan (2007 a, b). It could be argued that rising (adiabatically) thermals in the Martian boundary layer lose their buoyancy earlier, due to the radiative heating of the ambient air. Consequently, they are gradually slowed and stopped in the interfacial layer without triggering stronger temperature discontinuity at the top of the Martian boundary layer. As a result, the interfacial layer is relatively deep and difficult to differentiate from the inversion layer above it.

The potential temperature jump, $\Delta\Theta$, in the terrestrial boundary layer can be evaluated based on the following time-rate equation (e.g., Sorbjan, 1989):

$$\frac{d\Delta\Theta}{dt} = \Gamma \left(\frac{dz_c}{dt} - w_s \right) - \left(\frac{d\Theta_m}{dt} \right) \quad (2)$$

where Θ_m is the mean temperature in the mixed layer, Γ is the temperature gradient in the free atmosphere, and w_s is the large scale subsidence velocity, z_c is the height of the convective boundary layer. The value z_c can be assessed by adopting idealization that for $z < z_c$ the potential temperature is constant with height, and for $z > z_c$ the temperature gradient Γ is constant, and that the depth of the interfacial layer can be neglected.

The first term on the right-hand side of (2) describes the change of $\Delta\Theta$ due to the growth of the mixed layer. The second term reflects the changes of $\Delta\Theta$ due to turbulent and radiative heating of the mixed layer. Assuming that the potential temperature gradient in the interfacial

layer and in the layer above it are not significantly different, implies that $\Delta\Theta = 0$. For this value and for the subsidence velocity $w_s = 0$, Equation (2) can be rewritten as:

$$\frac{dz_c}{dt} = \frac{1}{\Gamma} \frac{d\Theta_m}{dt} \quad (3)$$

The values of the mixing height z_c as a function of local time can be obtained by integration of Eq. 3. Note that in the above equation, both Γ and $d\Theta_m / dt$ depend on time.

In order to evaluate the mixing height from Eq. (3), we picked a number of profiles in two ranges of summer sols, 660 - 680 ($L_s = 322^\circ - 333^\circ$), and 50 - 60 ($L_s = 354^\circ - 359^\circ$), and sorted them according to a local time. The use of multiple sols to construct a single diurnal cycle was validated by comparing the profiles from the same local time for each season, i.e., near noon and later afternoon. We found that profiles are repeatable and differ by no more than 1 K below 1 km, and by 1 - 2 K between 1 and 2 km. The temperature gradient Γ was then evaluated between levels of 1 and 2 km as a function of local time. The mean temperature Θ_m for a given profile was assessed by taking the average of temperatures between 0.2 km and 0.6 km. The time rate $d\Theta_m / dt$ was computed by fitting a quadratic polynomial to the mean values as a function of local time, and using the analytical derivative of the polynomial. The scatter about the quadratic fit was typically about 1%. Equation (3) was then solved by using a trapezoid rule integration, with the initial condition $z_c = 200$ m at 9 h LTST. The results are depicted in Figure 8.

As would be expected, both curves in Figure 8 nearly coincide. The figure shows a rapid growth of the well-mixed layer, by about 1 km/h during the interval from 9:00 to 10:00 LTST. The growth rate during the next 3 hours is even larger, equal to about 2 km/h. In the interval from 9:00 to 13:00 LTST, the summer well-mixed layer grows up to a level of about 7 km, which is in general agreement with the results of Hinson et al. (2008).

3.3. Heat flux

The Mini-TES observations allow the indirect evaluation of the turbulent heat flux profiles in the daytime boundary layer. The indirect method is based on the horizontally homogeneous equation for the potential temperature in the following form (e.g., Sorbjan, 1995):

$$\frac{\partial\Theta}{\partial t} = -\frac{\partial H}{\partial z} + \varepsilon_R \quad (4)$$

where $\partial\Theta/\partial t$ is the total heating rate, $\varepsilon_R = -\partial R/\partial z$ is the radiative heating rate, R is the net radiative flux, and H is the turbulent heat flux generated by convection.

Averaging Equation (4) in time, within interval from t_1 to t_2 , and then integrating the result with respect to height, yields:

$$\overline{H}(z) = \overline{H}_o - \int_0^z \left[\frac{\delta\Theta}{\delta t} - \overline{\varepsilon_R} \right] dz \quad (5)$$

or

$$\overline{H}(z) - \overline{H}(z_i) = \int_z^{z_i} \left[\frac{\delta\Theta}{\delta t} - \overline{\varepsilon_R} \right] dz \quad (6)$$

where \overline{H} is the time-averaged turbulent flux, $\delta\Theta = \Theta_2 - \Theta_1$, $\delta t = t_2 - t_1$, and z_i is the level near the top of the boundary layer, where the heat flux is most negative. The approach was previously tested by Sorbjan (1995), based on the large-eddy simulations of the atmospheric boundary layer on Earth.

The first integral is performed from the underlying surface up to the actual height z , and requires that value of the surface heat flux \overline{H}_o is known. The second integration is calculated from the actual height z up to level z_i . Assuming in (6) that $\overline{H}(z_i) = -r \overline{H}_o$, where r is a non-negative parameter, yields:

$$\overline{H}_o = \frac{1}{(1+r)} \int_0^{z_i} \left[\frac{\delta\Theta}{\delta t} - \overline{\varepsilon_R} \right] dz \quad (7)$$

$$\bar{H}(z_i) = -\frac{r}{(1+r)} \int_0^{z_i} \left[\frac{\delta\Theta}{\delta t} - \bar{\varepsilon}_R \right] dz$$

The numerical experiments of Sorbjan (2007 a, b) indicated that r is about 0.2.

Note that in the nocturnal conditions the temperature gradient near the surface is very large, the velocity gradient is expected to be small. In such conditions the Richardson number is large and most likely overcritical. Consequently, the turbulence flux divergence should be negligible, and the temperature changes of air enforced only by radiative effects. As a result an analysis based on (4) at night is problematic.

We employed Eqs. (7) and (6) to calculate the temperature flux on sol 56 ($L_s = 358^\circ$), based on temperature profiles in thirteen 200-second segments, beginning at 10:03 LTST. The total rate $\delta\Theta / \delta t$ was evaluated as a mean of differences between adjoining intervals, divided by the time step. We experimented with a variety of sampling intervals and time steps δt and found the 200-second adjoining intervals to be optimal. The values of $\bar{\varepsilon}_R$ were calculated using a radiative transfer model for the retrieved temperature profile and dust optical depth, while the wavelength dependence of the aerosols and the surface reflectance was taken from the literature (i.e., Arvidson et al., 2004; Wolff et al., 2006). We located the top of the convective layer z_i at the level, where the integrand ($\delta\Theta / \delta t - \bar{\varepsilon}_R$) was approximately equal to zero.

Figure 9a depicts both integrated terms in Eq. (6), the rate $\delta\Theta / \delta t$ and the radiative heating rate $\bar{\varepsilon}_R$. Figure 9b shows the heat flux profile, obtained by “top-down” integration of Equation (5). The resulting surface flux H_o is equal to about 0.8 K m s^{-1} . The heat flux in the figure increases with height, reaches a peak value of about 1.0 K m s^{-1} at a level of about 150 m, and decreases to -0.2 K m s^{-1} at a level of 1750 m. Taking into consideration that the product $c_p\rho$ is equal to $11 \text{ J K}^{-1}\text{m}^{-3}$, the resulting dynamic surface heat flux is $F_o = c_p\rho H_o = 8.8 \text{ W/m}^2$ and the entrainment flux $\bar{H}(z_i)$ is equal to about -0.2 K m s^{-1} .

During the Viking and Pathfinder missions, the surface heat flux on Mars was evaluated based on the drag law formulation, $F_o = c_p\rho C_H u_3 (T_1 - T_2)$, where C_H is the drag coefficient, and T_1, T_2, u_3 are values of the temperature and wind velocity at three levels in the Martian surface

layer. The composite values of Wilson and Joshi (2000) showed the surface heat flux F_o of about 10 W/m^{-2} , which tentatively agrees with our result. The daily maximum values of F_o for the Mars Pathfinder observations were about $10 - 15 \text{ W m}^{-2}$ (Savijarvi, 1999, Sutton et al., 1978). The Viking-1 Lander data indicated the maximum value of the flux F_o equal to about 25 W m^{-2} at local noon (Wilson and Joshi, 2000). The estimation of Martinez et al. (2009) for sols 25-26 of the Pathfinder mission, based on the Monin-Obukhov similarity theory, gives the flux of $2 - 5 \text{ W/m}^2$ at 10:00, and the daily maximum value of $6 - 10 \text{ W/m}^2$.

Note that in addition, a second heat flux profile is displayed in Figure 9b. The profile was obtained by the “bottom-up” integration, based of Eq. 5. This approach does not entail specification of the entrainment flux H_i , but requires a known value of the surface flux H_o . We specified the surface heat flux H_o using a value, computed based on a boundary-layer model by Savijarvi and Kauhanen (2008), for the appropriate sol and aerosol loading value. As seen in the figure, the resulting “bottom-up” flux is about 0.85 K m s^{-1} at the surface, reaches a maximum of about 1.1 K m s^{-1} at a level of about 150 m. It decreases above, and takes negative values above level of 1100 m. Both flux profiles in Figure 9b are generally in agreement with the heat flux profile calculated numerically by Savijarvi et al. (2004). The “bottom-up” profile implies that the most negative flux occurs at $z_i = 2000 \text{ m}$. The “top-down” heat flux profile in Figure 9 indicates that $z_i = 1800 \text{ m}$.

The characteristic peak of the turbulent flux profile within 200 m above the surface has previously been detected in numerical simulations (Savijarvi, 1991; Haberle et al., 1993b; Savijarvi et al., 2004). As it follows from Eq. (4), when $\partial H / \partial z > 0$ near the underlying surface, convection contributes to the cooling of the surface layer. Because the flux divergence $\partial H / \partial z$ near the surface is quite large, a sub-layer where the heat flux could be assumed approximately constant with height, is very shallow. Figure 9b indicates that a 10% increase of the heat flux (from H_o to $1.1H_o$) takes place in a layer about 5 m deep. This allows us to conclude that the Monin-Obukhov similarity during morning convection on Mars is valid only in a layer of only a few meters above the ground.

4. Conclusions

We have presented and discussed vertical profiles of the potential temperature on Mars, collected within the first 702 sols of operation by the Mini-TES spectrometer, located on-board the MER Spirit rover. Retrieved temperature profiles were obtained using a slightly modified form of the original retrieval procedure of Smith et al. (2006), which allowed for the removal of artifacts associated with the inaccuracy of initial guesses in the retrieval scheme at certain times of day. Because we found the retrieved Mini-TES potential temperature profiles to have some sensitivity to the value of the elevation angle, our analyses were limited to cases with relatively large values of the elevation angle (more than 20° above the horizon), where uncertainties are expected to be smallest.

The Mini-TES retrievals considered here allowed the appraisal of the diurnal and seasonal variation of potential temperature in the lower part of the Martian boundary layer, evaluation of the boundary-layer growth with time, and the computation of the turbulent heat flux. We observed that daytime potential temperature profiles gradually evolved during the daytime toward higher temperatures, as a result of the absorption of long-wave radiation and convective mixing, generated by a hot underlying surface. At night, the temperature profiles evolved with time toward lower temperatures, mainly due to radiative cooling, as the nocturnal turbulence is expected to be generally sporadic or negligible.

We observed a lag between the occurrence of the diurnal maximum of the temperature near the ground and the potential temperature at higher levels. The lag can be explained by the relatively low thermal inertia of Martian soil, which causes the near-surface air temperature to almost instantly react to the level of solar insolation. As a result of strong convective mixing, the maximum potential temperature near the surface was found to be only slightly higher than at a level of 2 km. The minimum potential temperature near the surface was observed at about sunrise. The lack of mixing at night caused that the minimum potential temperature near the surface was significantly lower than at a level of 1 km.

The day-time potential temperature decreased during the period from the beginning of Spirit operations until approximately the Southern Hemisphere Winter Solstice, and then warmed up in the interval between the Southern Hemisphere Spring Equinox and the Southern Hemisphere Summer Solstice. Subsequently, the potential temperature was decreased again. We

found a quite good agreement in the temperatures at the beginning of years 1 and 2, except the first few sols of both years, for which the difference was about 5 K. The differences were most likely associated with large dust-storm events.

No evidence of the temperature discontinuity (jump) was found at the top of the Martian boundary layer. This fact could be associated with a relatively large depth of the interfacial layer, which was difficult to differentiate from the inversion layer above it. We assessed the height of the daytime boundary layer, and found its growth to be about 1 - 2 km/h in the interval from 9:00 to 14:00 LTST.

We found (using the “top-down” integration) that the retrieved heat flux, at about 10:00 LTST on sol 56, increased with height from about 8.8 W m^{-2} at the surface to a maximum value of about 11 W m^{-2} at 150 m height, and then gradually decreased to about -2.2 W m^{-2} at a level of about 1750 m. We concluded that Monin-Obukhov similarity on Mars during daytime convection is valid in a shallow layer only a few meters deep above the surface.

At the time of this writing, both MER spacecraft still continue to operate on the surface of Mars. However, the utility of the Mini-TES observations for atmospheric temperature profiling has been essentially eliminated due to dust contamination of the optical elements. Spirit’s record may provide some insights well into a second year of Mars observations. Opportunity’s dataset appears to be limited to a single Martian year. Nevertheless, efforts continue to provide a better correction for the dust contamination, and thus potentially extend the MER record of boundary layer temperatures.

Acknowledgements

We thank Professor Hannu Savijarvi for graciously allowing us to use his single-column Martian model. We are grateful to four anonymous reviewers for their helpful comments. The performed research has been supported by NASA through the Mars Exploration Rover Project, a portion of which was carried out at the Jet Propulsion Laboratory, California Institute of Technology, under a contract with the National Aeronautics and Space Administration.

References

- Arvidson, RE, Anderson RC, Bartlett P, Bell III JF, Blaney D, Christensen PR, Chu P, Crumpler L, Davis K, Ehlmann BL, Fergason R, Golombek MP, Gorevan S, Grant JA, Greeley R, Guinness EA, Haldemann AFC, Herkenhoff K, Johnson J, Landis G, Li R, Lindemann R, McSween H, Ming D W, Myrick T, Richter L, Seelos IV FP, Squyres SW, Sullivan RJ, Wang A, Wilson J. 2004. Localization and Physical Properties Experiments Conducted by Spirit at Gusev Crater, *Science*, **305**: 821 – 824.
- Christensen, PR, Ruff SW, Fergason RL, Knudson AT, Anwar TS, Arvidson SRE., Bandfield JL, Blaney DL, Budney C, Calvin WM, Glotch TD, Golombek MP, Gorelick N, Graff TG, Hamilton VE, Hayes A, Johnson JR, Mc Sween Jr HY, Mehall GL, Mehall LK, Moersch JE, Morris RV, Rogers AD, Smith MD, Squyres SW, Wolff MJ, Wyatt MB. 2004. Initial Results from the Mini-TES Experiment in Gusev Crater from the Spirit Rover. *Science*, **6**: 837 - 842.
- Haberle RM, Pollack JB, Barnes JR, Zurek RW, Leovy CB, Murphy JR, Schaeffer J, Lee H. 1993a. Mars atmospheric dynamics as simulated by the NASA/Ames general circulation model, 1: The zonal mean circulation. *J. Geophys. Res.*, **102**: 13301-13311.
- Haberle, RM, Houben HC, Hertenstein R, Herdtle T. 1993b. A boundary-layer model for Mars: Comparisons with Viking lander and entry data. *J. Atmos. Sci.*, **50**: 1544-1559.
- Hinson D P, Simpson RA, Twicken JD, Tyler GL, Flasar FM. 1999. Initial Results from Radio Occultation Measurements with Mars Global Surveyor, *J. Geophys. Res. (Planets)*, **104**: 26297-27012.
- Hinson DP, Tyler GL, Hollingsworth JL, Wilson RJ. 2001. Radio occultation measurements of forced atmospheric waves on Mars, *J. Geophys. Res. (Planets)*, **106**: 1463-1480.
- Hinson DP, Pätzold M, Tellmann S, Häusler B, Tyler GL. 2008. The depth of the convective boundary layer on Mars. *Icarus*, **198**: 1, 57-66.
- Kliore AJ, Fjeldbo G, Seidel BL, Sykes MJ, Woiceshyn PM. 1973. S Band Radio Occultation Measurements of the Atmosphere and Topography of Mars with Mariner 9: Extended Mission Coverage of Polar and Intermediate Latitudes, *J. Geophys. Res.*, **78**: 4331–4351.
- Lindal GHB, Hotz DN, Sweetnam Z, Shippony JP, Bernkle GV, Hartsell RT, Spear WH, Michael WH. 1979. Viking radio occultation measurements of the atmosphere and topography of Mars: Data acquired during 1 Martian year of tracking. *J. Geophys. Res.*, **84**: 8443–8456.
- Martinez G, Valero F, Vazquez L. 2009. Characterization of the Martian Surface Layer. *J. Atmos. Sci.*, **66**, 187-198. Michaels TI., Rafkin SCR. 2004. Large-eddy simulation of atmospheric convection on Mars. *Q. J. R. Meteorol. Soc.*, **130**: 1251-1274.

- Rafkin SCR, Haberle RM, Michaels TI. 2001. The Mars regional atmospheric modeling system: model description and selected simulations. *Icarus*, **151**: 228-256.
- Savijärvi H. 1991. A model study of the PBL structure on Mars and Earth, *Beitr. Phys. Atmos.*, **64**: 219-229.
- Savijärvi H, Määttänen A, Kauhanen J, Harri A-M, 2004. Mars Pathfinder: New data and new model simulations. *Q.J.R. Meteorol. Soc.*, **130**: 669-683.
- Savijärvi H, Kauhanen J. 2008. Surface and boundary-layer modelling for the Mars Exploration Rover sites. *Q. J. R. Meteorol. Soc.*, **134**: 635 - 641.
- Schofield, JT, Barnes JR, Crisp D, Haberle RM, Larsen S, Magalhes JA, Murphy JR, Seiff A, Wilson G. 1997. The Mars Pathfinder Atmospheric Structure Investigation/ Meteorology (ASI/MET) experiment. *Science*, **278**: 1752-1758.
- Smith, M.D., Wolff, MJ Lemmon MT, Spanovich N, Banfield D, Budney CJ, Clancy RT, Ghosh A, Landis GA, Smith P, Whitney B, Christensen PR, Squyres SW. 2004: First atmospheric science results from the Mars exploration rovers Mini-TES. *Science*, **306**: 1750-1753.
- Smith MD, Wolff MJ, Spanovich N, Ghosh A, Banfield D, Christensen PR, Landis GA, Squyres SW. 2006: One Martian year of atmospheric observations using MER Mini-TES, *J. Geophys. Res.*, **111**: E12S13.
- Smith MD. 2008. Spacecraft observations of the Martian atmosphere. *Annu. Rev. Earth Planet Sci.* **36**: 191-219.
- Sorbjan Z 1995. Toward evaluation of heat fluxes in the convective boundary layer. *J. Appl. Meteor.* **34**: 1092-1098.
- Sorbjan Z. 2007a. Statistics of shallow convection on Mars based on large-eddy simulations. Part 1: Windless conditions. *Boundary-Layer Meteorol.*, **123**: 121-142.
- Sorbjan Z. 2007b. Statistics of shallow convection on Mars based on large-eddy simulations. Part 2: Effects of wind. *Boundary-Layer Meteorol.*, **123**: 143-157.
- Spanovich N, Smith MD, Smith PH, Wolff MJ, Christensen PR, Squyres SW. 2006. Surface and near-surface atmospheric temperatures from the Mars Exploration Rover landing sites. *Icarus*, **180**: 314–20.
- Sutton JL, Leovy CB, Tillman JE. 1978. Diurnal variation of the Martian surface layer meteorological parameters during the first 45 sols at two Viking lander sites, *J. Atmos. Sci.*, **35**: 2346-2355.
- Tillman JE, Johhson, NC, Guttorp, P, Percival, DB 1994. The Martian annual atmospheric pressure cycle – Years without great dust storms. *J. Geophys. Res.*, **98**:6, 10963-10971.

- Toigo AD, Richardson MI, Ewald SP, Gierasch PJ. 2003. Numerical simulation of Martian dust devils. *J. Geophys. Res.*, **108**: 6, 1-14.
- Wilson GR, Joshi M. 2000. The Martian surface boundary layer. 31st Annual Lunar and Planetary Science Conference, March 13-17, 2000, Houston, Texas.
- Wolff MJ, Clancy RT, Smith MD, Arvidson RE, Cantor B, Kahre M, Morris R, Seelos F. 2007. Investigating the Wavelength Dependence of the Single-Scattering Albedo of Martian Dust Aerosols with CRISM and MARCI Observations of the Very Dusty Atmosphere in 2007, *Eos Trans. AGU*, **88**(52), Fall Meet. Suppl., Abstract P31D-03.
- Wolff MJ, Smith MD, Clancy RT, Arvidson RE. 2008. Properties of Martian Dust Aerosols From the Combination of MER and MGS/MRO Observations. *Eos Trans. AGU*, **89** (53), Fall Meet. Suppl., Abstract. P33C-02.
- Wolff MJ, Smith MD, Clancy RT, Spanovich N, Whitney BA, Lemmon MT, Bandfield JL, Banfield D, Ghosh A, Landis G, Christensen PR, Bell JF, Squyres SW. 2006. Constraints on dust aerosols from the Mars Exploration Rovers using MGS overflights and Mini-TES. *J. Geophys. Res.*, **111**: E12S17.

List of Figures

Figure 1. Profiles of two-second averaged potential temperature, plotted every 100 s beginning at 8:50 LTST on sol 53 ($L_s = 356^\circ$): (a) the primary profiles, (b) the corrected profiles (see text).

Figure 2. Profiles of the potential temperature detected on sol 7 for different elevation angles: $\beta = 10^\circ$ (13:04 LTST), 20° (13:09 LTST), and at 30° (13:13 LTST).

Figure 3. Diurnal variation of the potential temperature profiles: (a) the daytime profiles on sol 53, (b) the afternoon and nocturnal profiles on sols 49, 53, 55, 65, and 70. The dotted line indicates the “instantaneous” trajectory of a thermal.

Figure 4. The afternoon and nocturnal profiles of the potential temperature on sol 180.

Figure 5. The diurnal distribution of the potential temperature at three levels 20 m, 1 km, and 2 km, derived from plots in Figure 3.

Figure 6. Profiles of the potential temperature detected at about: (a) 13:00 LTST, and (b) 16:00 LTST, for selected sol numbers.

Figure 7. The temporal distribution of the potential temperature of air at about 16:00 LTST, at three levels: 20 m, 1 km, and 2 km. The names of equinoxes and solstices refer to the Southern Hemisphere.

Figure 8. Estimated values of the convective boundary layer height z_c for sols 50 - 60 ($L_s = 354^\circ - 359^\circ$), and 660-680 ($L_s = 322^\circ - 333^\circ$).

Figure 9. Profiles of: (a) the total $\partial\Theta/\partial t$ and radiative $\overline{\varepsilon_R}$ heating rates, and (b) the resulting mean heat flux profiles, obtained by bottom-up integration from a given value H_o at the surface, and by top-down integration, at 10:04 LTST on sol 56.

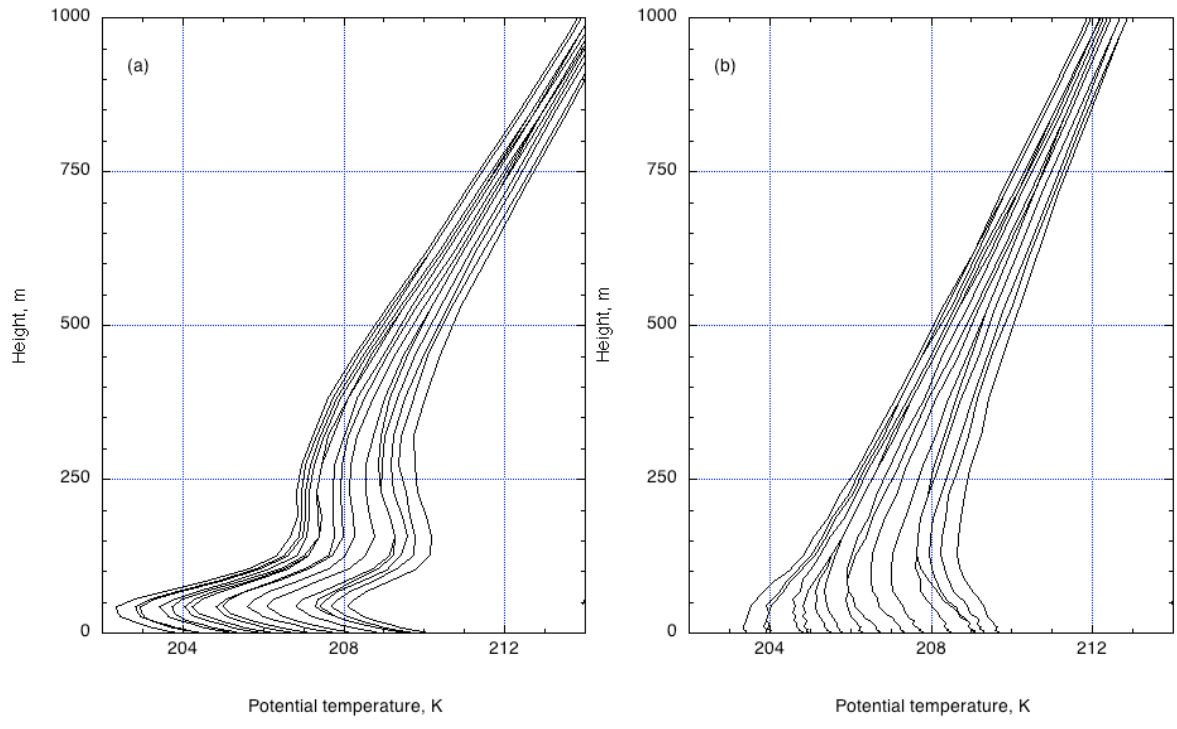


Fig. 1a, b

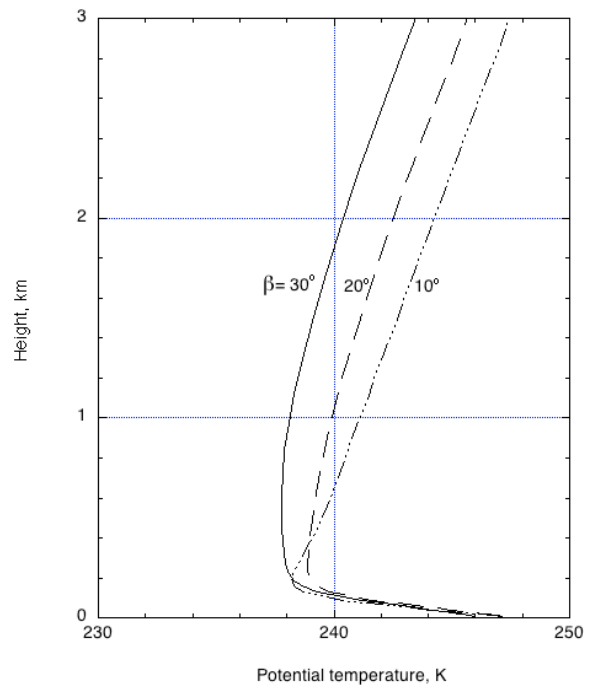


Fig. 2

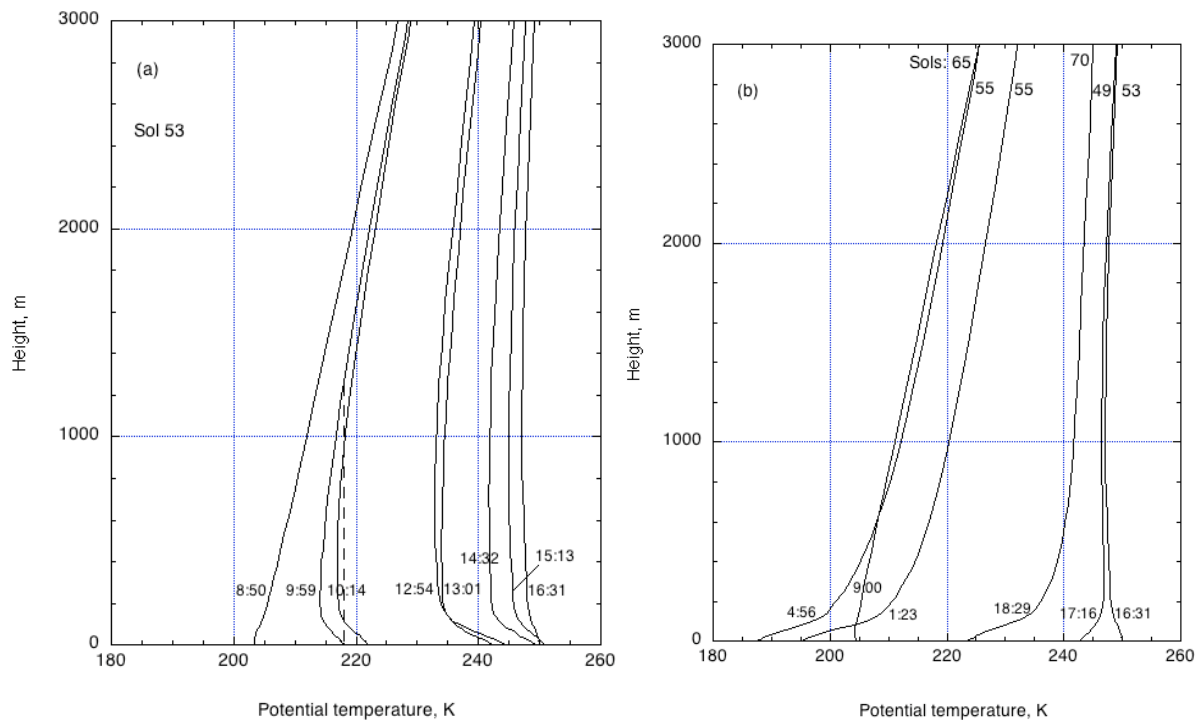


Fig. 3a, b

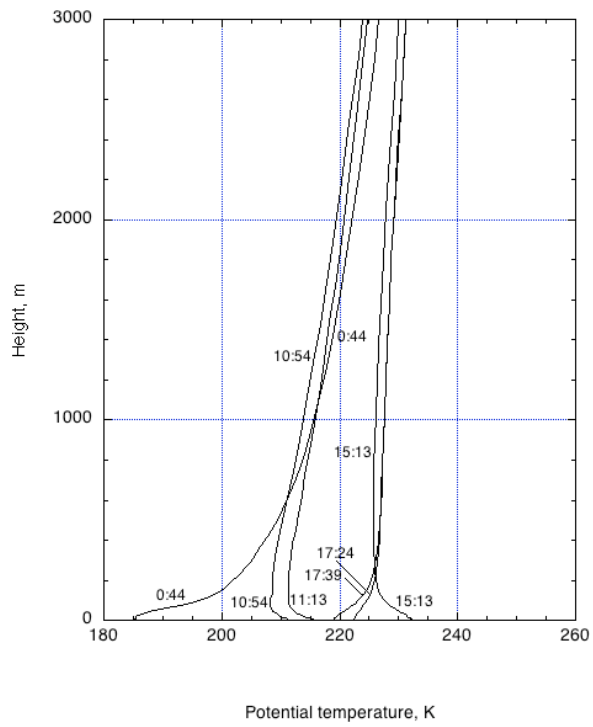


Fig. 4

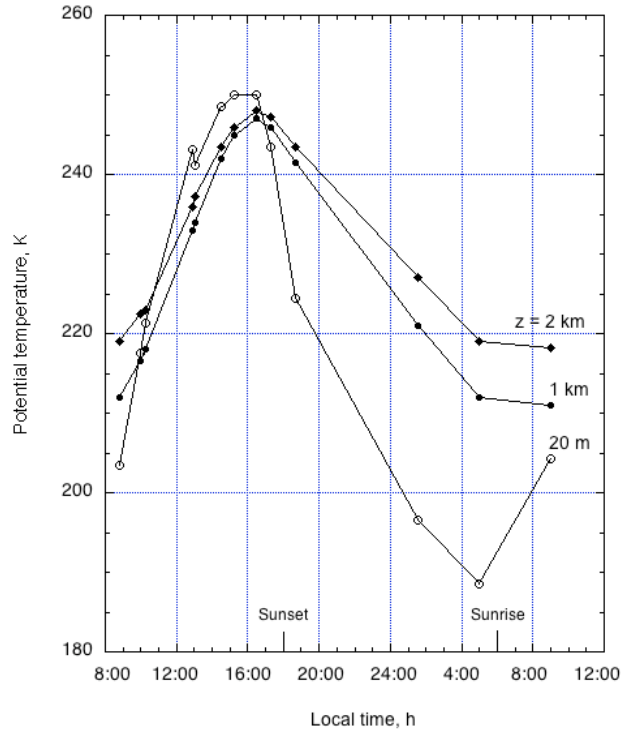


Fig. 5

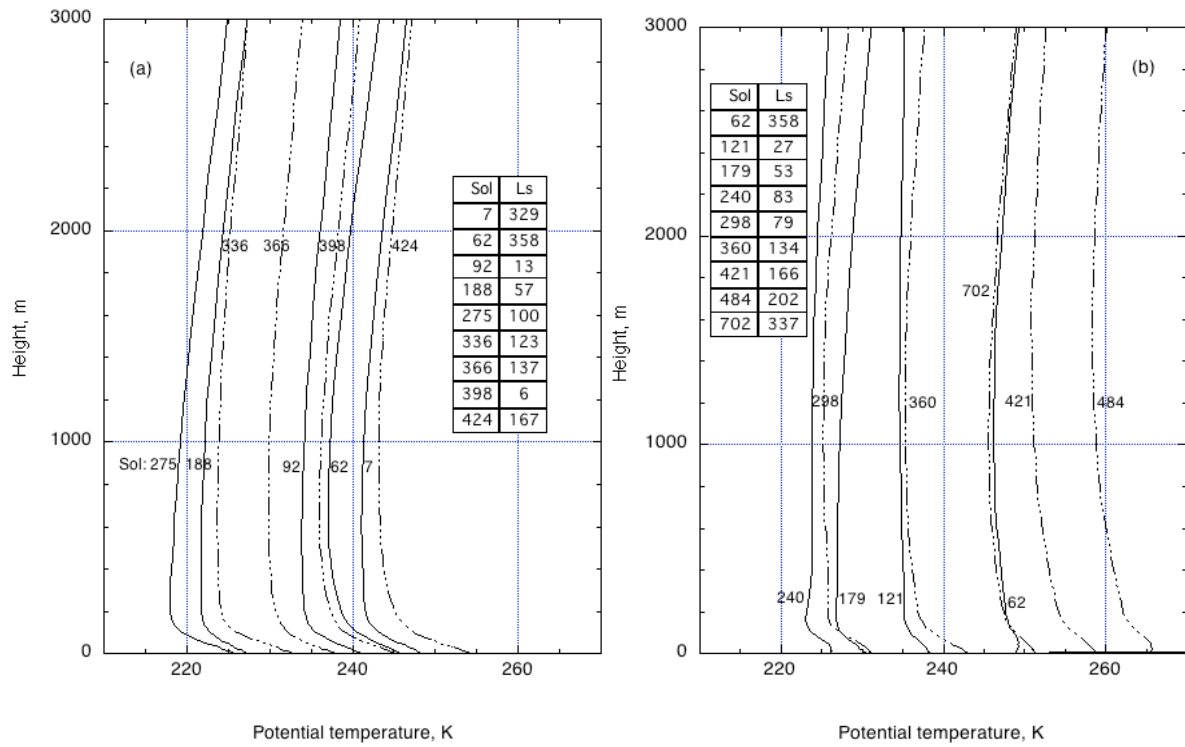


Fig. 6a, b

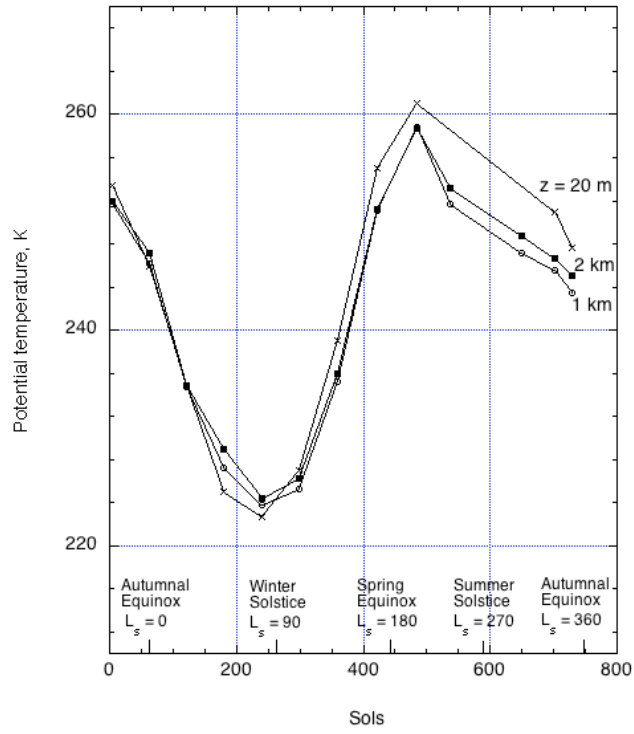


Fig. 7

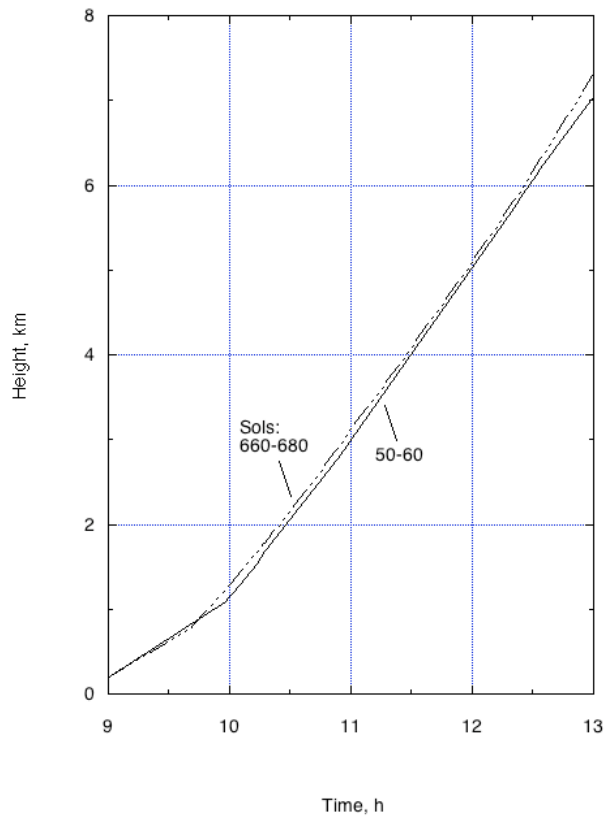


Fig. 8

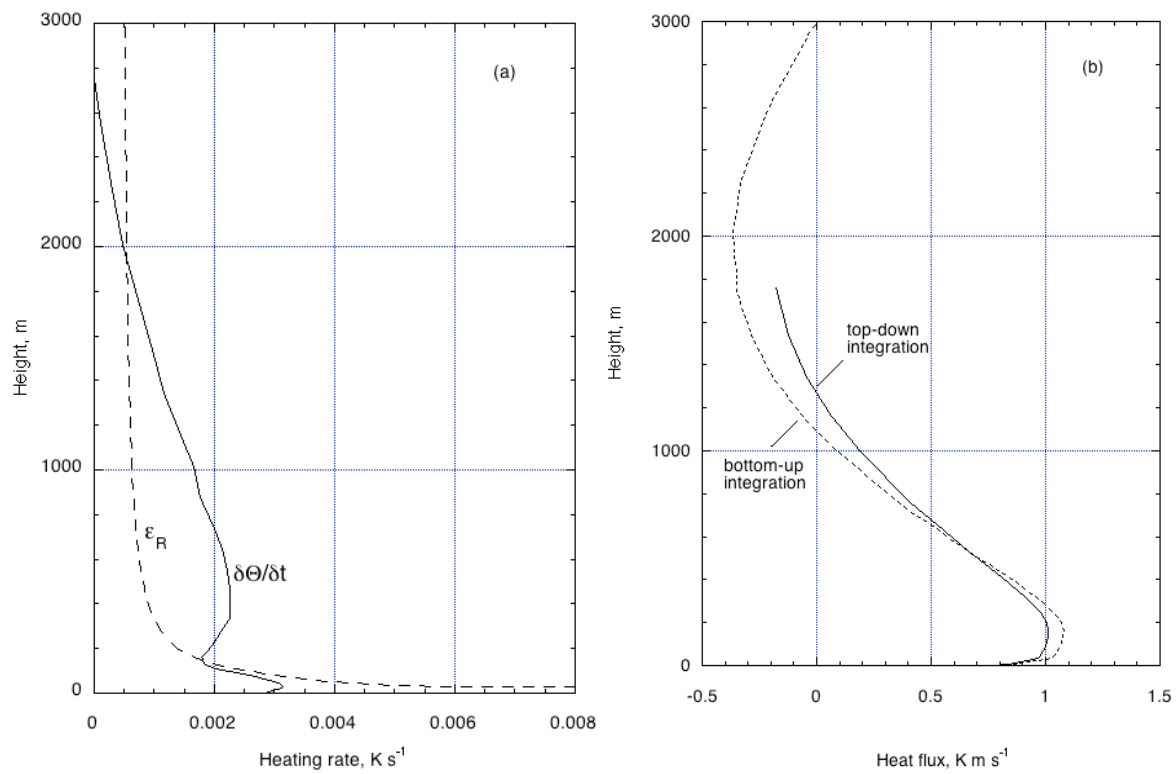


Fig. 9a, b